Low-Power Wearable Systems for Continuous Monitoring of Environment and Health for Chronic Respiratory Disease

James Dieffenderfer, Henry Goodell, Steven Mills, Michael McKnight, Shanshan Yao, Feiyan Lin,
Eric Beppler, Brinnae Bent, Bongmook Lee, Veena Misra, Yong Zhu, Omer Oralkan,
Jason Strohmaier, John Muth, David Peden, and Alper Bozkurt

Abstract—We present our efforts toward enabling a wearable sensor system that allows for the correlation of individual environmental exposures with physiologic and subsequent adverse health responses. This system will permit a better understanding of the impact of increased ozone levels and other pollutants on chronic asthma conditions. We discuss the inefficiency of existing commercial off-the-shelf components to achieve continuous monitoring and our system-level and nano-enabled efforts toward improving the wearability and power consumption. Our system consists of a wristband, a chest patch, and a handheld spirometer. We describe our preliminary efforts to achieve a submilliwatt system ultimately powered by the energy harvested from thermal radiation and motion of the body with the primary contributions being an ultralow-power ozone sensor, an volatile organic compounds sensor, spirometer, and the integration of these and other sensors in a multimodal sensing platform. The measured environmental parameters include ambient ozone concentration, temperature, and relative humidity. Our array of sensors also assesses heart rate via photoplethysmography and electrocardiography, respiratory rate via photoplethysmography, skin impedance, three-axis acceleration, wheezing via a microphone, and expiratory airflow. The sensors on the wristband, chest patch, and spirometer consume 0.83, 0.96, and 0.01 mW, respectively. The data from each sensor are continually streamed to a peripheral data aggregation device and are subsequently transferred to a dedicated server for cloud storage. Future work includes reducing the power consumption of the system-on-chip including radio to reduce the entirety of each described system in the submilliwatt range.

J. Dieffenderfer, H. Goodell, and B. Bent are with the Department of Biomedical Engineering, North Carolina State University, Raleigh, NC 27606 USA (e-mail: jpdieffe@ncsu.edu; hpgoodel@ncsu.edu; bmbent@ncsu.edu).

S. Mills, M. McKnight, F. Lin, E. Beppler, B. Lee, V. Misra, O. Oralkan, J. Strohmaier, J. Muth, and A. Bozkurt are with the Department of Electrical Engineering, North Carolina State University, Raleigh, NC 27606 USA (e-mail: scmills2@ncsu.edu; mdmckni2@ncsu.edu; flin4@ncsu.edu; ecbepple@ncsu.edu; blee2@ncsu.edu; vmisra@ncsu.edu; ooralka@ncsu.edu; jmstrohm@ncsu.edu; muth@ncsu.edu; aybozkur@ncsu.edu).

S. Yao and Y. Zhu are with the Department of Mechanical and Aerospace Engineering, North Carolina State University, Raleigh, NC 27606 USA (e-mail: syao2@ncsu.edu; yzhu7@ncsu.edu).

D. Peden is with the Center for Environmental Medicine, Asthma, and Lung Biology, University of North Carolina, Chapel Hill, NC 27599 USA (e-mail: david_peden@med.unc.edu).

Color versions of one or more of the figures in this paper are available online at http://ieeexplore.ieee.org.

Digital Object Identifier 10.1109/JBHI.2016.2573286

Index Terms—Environmental and physiological sensing, wearable asthma monitoring.

I. INTRODUCTION

ENVIRONMENTAL factors are increasingly appreciated as important determinants of human health. To fully monitor and manage chronic diseases, it is crucial to understand the effect of exposure to environmental stressors on various physiologica parameters, which ultimately increase disease morbidity and mortality. Management of these conditions currently focuses on frequent visits to a healthcare facility, during which lifestyle changes and medications are prescribed based on a recollection of health events by patients and a limited number of metrics, most of which are measured during the visit and not in a person's home or work setting. Thus, treatment recommendations are made on the basis of patient (or caregiver) recall of signs and symptoms with very little objective physiological or behavioral data from the patient in real time. Respiratory diseases are perfect examples of chronic diseases currently managed in this way. Asthma is one of the most common of these diseases, affecting one in twelve people (approximately 25 million individuals in the United States alone), which in 2007, resulted in 56 billion dollars of medical expenses and thousands of preventable deaths [1].

Current asthma treatment guidelines recommend that objective measures of lung function can be obtained in a clinic by spirometry, in which the forced expiratory volume in 1 s (FEV1), peak expiratory flow (PEF), and forced vital capacity (FVC) are assessed [2]. However, measurements of lung function are usually not available during acute exacerbations of asthma, as these typically do not occur at a health care facility where standard spirometry is available. Exposure to pollutants or cold, dry air is known to trigger acute asthma attacks and often impact the patient several hours to several days after exposure. The ability to monitor lung function over long periods of time with corresponding local environmental factors in persons with asthma and other chronic respiratory diseases would help clinicians define an individual's susceptibility to environmental stressors. This would allow for directing increased asthma treatment or preventing adverse outcomes in asthmatics following exposure to environmental stressors, greatly improving management of the disease. Epidemiologic studies suggest an extremely high correlation between ozone exposure and the condition of an asthma patient's lung function [3]. While the existence of this

relationship is widely accepted, the exact mechanism is complex in nature and a subject of active research. The previous literature has shown that using geographical estimates of ozone, as opposed to personal ozone exposure, results in poor correlation, necessitating a device with the means of measuring ozone [4]. In addition to ozone, we have also chosen volatile organic compounds (VOCs) as target analytes for detection as the correlation between exposure to domestic VOCs and the risk of developing and/or exacerbating asthma and allergies is an important topic requiring additional research [5].

Current continual monitoring systems for asthma patients include devices that monitor heart rate and respiratory rate [6], the use of a GPS to track the patient's exposure to polluted areas [7], and a few consumer products in early stages for tracking physiological parameters [6]; none of these integrate environmental and physiological sensors, especially to track the impact of ozone and VOCs on wellness. An assembled system combining these individual solutions becomes bulky, desynchronized, power-hungry, and difficult to use during daily activities thereby increasing the rejection probability by the user. Additionally, the inconvenience associated with frequently charging power sources warrants the need for a low-power system in tandem with energy harvesting in order to integrate these wearable devices into daily living routines.

Beyond respiratory diseases, the continuous monitoring of health and environment through wearable devices has the potential to create a paradigm shift in improving healthcare by empowering patients and doctors to transition from managing illness to managing wellness and outcomes. Under the National Science Foundation Nanosystems Engineering Research Center for Advanced Self-Powered Systems of Integrated Sensors and Technologies (ASSIST), we develop key core technologies for achieving a high-performance, multifunctional, self-powered environmental, and biomedical sensing system that targets maximizing the power harvested from the body in the form of heat and movement while simultaneously minimizing the power consumed via low-power sensing, subthreshold CMOS computation, novel transistor designs, and ultralow-power radios [8], [9]. In this paper, we investigate the feasibility of engineering a system for long-term, continuous monitoring of wellness status and of relevant environmental factors around those with respiratory problems, such as asthma, during their daily-life activities. In the scope of this study, we particularly focus on the two aspects that seem to be hindering the continuous monitoring during daily life: power consumption and wearability. Within the ASSIST Center, we have defined $500\ \mu\mathrm{W/cm^2}$ as an appropriate target for our energy harvesters and plan on being able to support 1 mW of power consumption [8]. While separate research is underway to develop an ultralow-power radio, system on chip (SoC), and thermoelectric devices to harvest thermal radiation from the body [8], [9], in this article, we report our efforts toward reducing the power levels of sensors and sensor front-end electronics to submilliwatt levels with our primary contributions being the development of an ultralow-power ozone sensor, VOC sensor, spirometer, and the integration of these and other sensors into a low-power health and environmental sensing platform. The paper outline is as follows: in Section II, we describe the general architecture of such a wearable system for
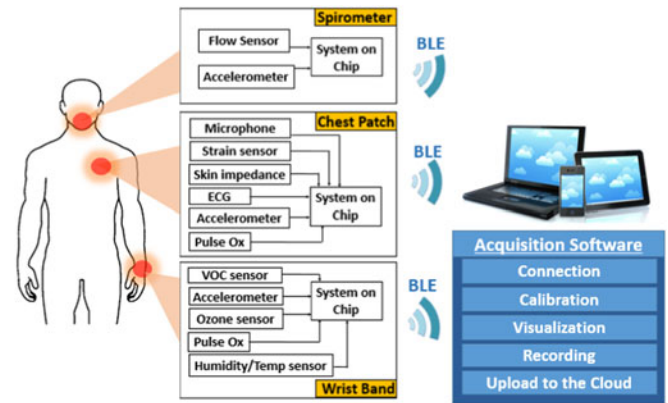

Fig. 1. System diagram of various sensors embedded in each form factor. All the platforms independently stream data to the data aggregator which then uploads it to a dedicated server using WiFi.
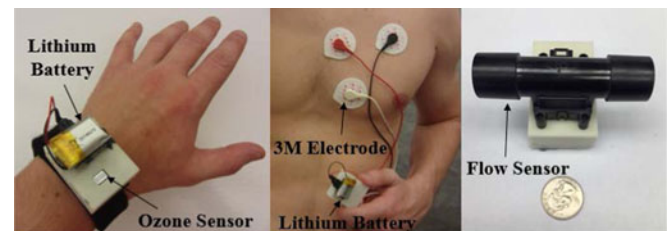

Fig. 2. Prototype system including the chest-patch, wristband and the spirometer assembled together using COTS components only.

simultaneous health and environment monitoring in the context of asthma management. In Section III, we present the challenges of using currently available commercial-off-the-shelf (COTS) components to establish such a system and present our efforts toward improving power consumption and wearability. Finally, in Section IV, we present preliminary results assessing the performance of our system tested in controlled environments. Our future direction is outlined in Section V along with a summary of our conclusions.

II. SYSTEM OVERVIEW

Toward the long-term goal of a completely self-powered sensor system, we present here a wearable multimodal sensor testbed that can simultaneously monitor the health and environment in the context of asthma management (see Fig. 1). We present a prototype system that was first entirely based on state-of-the-art COTS components which we later strategically and gradually replaced with custom components to improve the wearability and lower the power consumption to enable continuous monitoring. Including a chest-patch, wristband, and spirometer, this prototype is intended for monitoring the impact of ozone and VOC exposure on various respiratory-related physiological parameters including heart rate variability, respiratory rate variability, activity level, and wheezing. In this section, we describe the general architecture of the system. In the following section, the system and sensor improvements will be discussed that took the prototype from a relatively high-power system (see Fig. 2) to a low-power system (see Fig. 3).
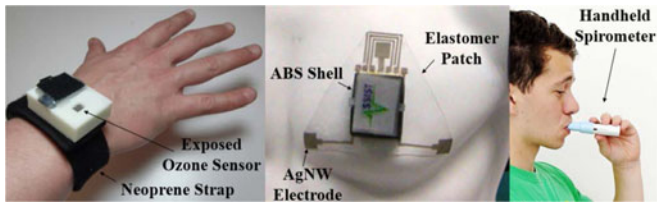
Fig. 3. Prototype system incorporating the custom ASSIST sensors. (Left) Neoprene wrist strap with ABS plastic shell containing the circuitry for measuring ozone concentration, PPG, motion, temperature, and humidity. (Center) Elastomer patch with ABS plastic shell containing circuitry for measuring ECG, skin impedance, PPG, wheezing, and motion. (Right) Handheld spirometer for measuring lung functionality.

Fig. 4. Exploded view of the wristband device, chest patch, and spirometer including the layers of the optical probe.

The system is comprised of three parts: a wristband, a chest patch, and a handheld spirometer. The wristband sensors track ozone exposure, ambient temperature, ambient relative humidity, photoplethysmography (PPG), and motion. The chest patch sensors are capable of measuring ECG, skin impedance, PPG, motion, and acoustic signals (see Fig. 1). The spirometer is capable of measuring FEV1, PEF, and FVC. In order to handle the immense amount of data being generated by these three devices, the system constantly transmits the recordings to a Bluetooth Low Energy (BLE)-enabled peripheral data aggregation device (e.g., a laptop, tablet computer, or smartphone).

The three wearable systems are synchronized by parallel reading of the three BLE connections by the data aggregator and the sorting of the data based on the timestamp associated with each BLE packet. Because each sensor has a different required sampling rate, BLE profiles were created on each device that group the sensors into either a fast or slow sampling rate. These profiles send packets independently of each other and the different sensor measurements are also synchronized using the packet timestamp in a similar fashion to the three wearable devices. The VOC sensor is sample at 0.02 Hz; Ozone, temperature, and humidity sensors on the wristband device are sampled at 10 Hz; PPG and the accelerometer are sampled at 30 Hz. On the chest patch, the PPG, accelerometer, and skin impedance are sampled at 30 Hz, while the ECG is sampled at 50 Hz and the microphone at 2 kHz. In the case of the spirometer, the device is powered on right before usage and establishes a BLE connection with the data aggregator (smartphone, tablet, or computer). The spirometer contains an accelerometer sampled at 30 Hz to determine the tilt of the device to help ensure that the user has the proper posture and performs a reproducible breathing maneuver when exhaling through the device. The airflow is sampled at a rate of 1 kHz using the microcontroller's built-in analog-to-digital converter (ADC). The data are time stamped and transmitted to the data aggregator where FEV1, PEF, and FVC are calculated. Once a substantial amount of data has been transferred to the data aggregator from each of the three subsystems, the information is then autonomously uploaded to a dedicated server on the cloud. This approach allows for the collection of a larger volume of data, which may be analyzed over large periods of time by the patients or patient-approved physicians.

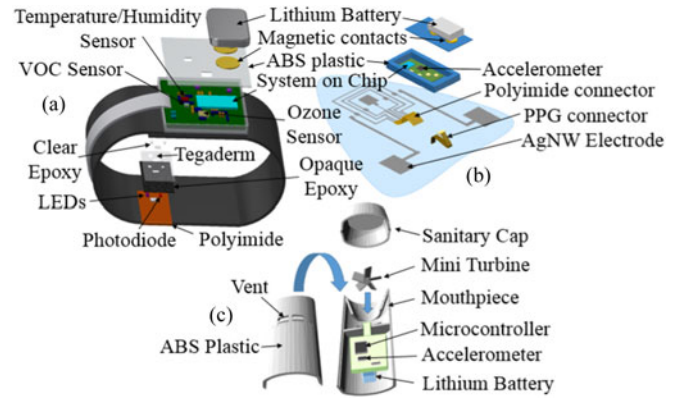The chest patch, wristband, and spirometer consist of printed circuit boards enclosed within three-dimensional (3-D)-printed shells made of ABS plastic (see Fig. 3). The wristband device is attached, via Velcro, to a strap made of Neoprene and secured around the patient's wrist. The plastic shell containing the chest patch circuit is affixed via a custom connector to the polymer patch. This makes the cleansing and disposal of the flexible patch and Neoprene wristband possible without affecting the circuitry. In the case of the spirometer, the mouthpiece can be cleaned with a small wipe for personal use. For this study, as multiple patients are using one device, a standard spirometry filter was placed in front of the mouthpiece.

The wristband and chest patch devices have a lithium-polymer battery affixed to the top of the plastic shell, while the spirometer has a smaller battery embedded within the shell (see Fig. 4). The terminals of the batteries are gold-plated circular magnets that provide physical and electrical connectivity. The wristband and chest patch both have magnetic receptacles that are soldered to the circuit using gold compatible solder. The voltage from the battery is subsequently connected to a voltage regulator to provide a stable 3-V supply voltage for the rest of the circuitry. All devices incorporate an SoC that has a built-in BLE radio.

In both the wristband and chest patch, the PPG probe is connected to the circuit board by means of a small ribbon cable. The probe is manufactured in-house by using a flexible copper-covered polyimide substrate. Once the traces are defined by printing wax ink as a resist and etching the copper, the soldered photodiode and light emitting diodes (LEDs) are surrounded by a coating of opaque epoxy. This layer electrically insulates the probe, provides a cushion for the edges of the optical elements, and acts as an optical barrier between the photodiode and LEDs. An additional coating of clear epoxy is subsequently added to further insulate the optical elements while still maintaining transparency (see Fig. 5).

III. SENSOR OPTIMIZATION

In this section, we present the particular state-of-the-art COTS components that we selected to construct our prototype, the limitations of each sensor type and our efforts to overcome these limitations by system-level strategies as well as novel nano-enabled technologies. All of the sensors, frontend circuits, processors,
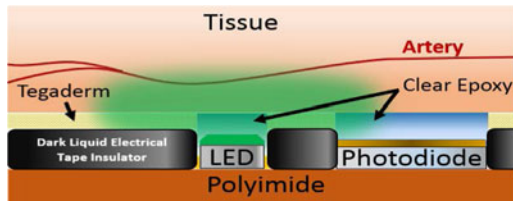
Fig. 5. Interface between the optical probe and the tissue. The optical probe is the same for both the wristband device and the chest patch. The coating of the liquid insulator, clear epoxy, and 3M Tegaderm is performed manually.
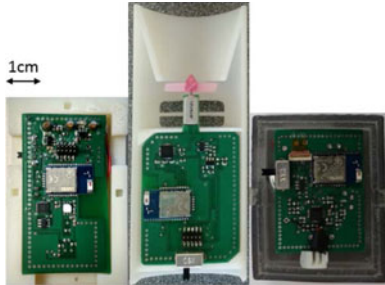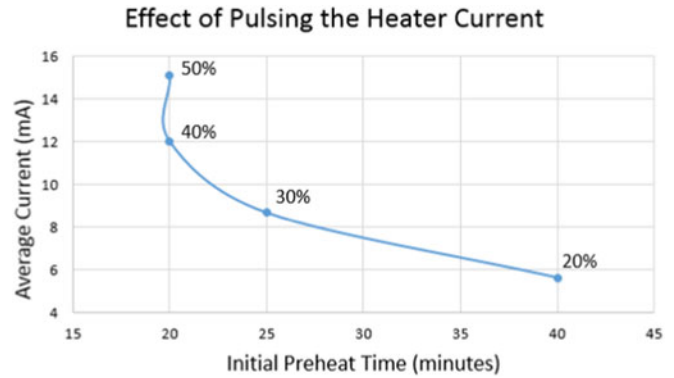

Fig. 7. Average current supplied to the ozone sensor was measured for an oscillating heater current of 2 kHz with varying duty cycle. Because of the relatively slow dissipation of the thermal energy on the heater, a duty cycle of 40% achieves similar results to that of a DC current. The preheat was performed in an open setting with the sensing element exposed to a typical amount of particulates.
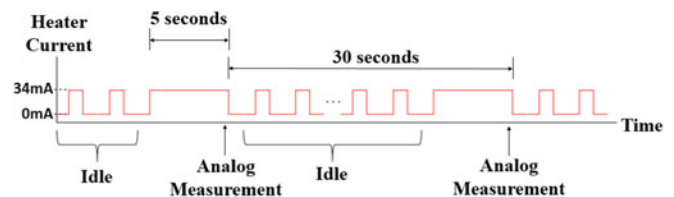

Fig. 6. Inside of the enclosure showing the electronics for the wristband (left), spirometer (middle), and chestpatch (right).

Fig. 8. Power saving scheme for driving the commercial metal oxide ozone sensor.

and receivers incorporated within the platform were selected considering a minimal overall power consumption within reasonable wearable form factors (see Fig. 6). The results are presented in the next section (see Fig. 6).

A. Ambient Gas Sensing

1) Ozone: COTS ozone sensors typically use either electrochemical or metal-oxide sensing methodologies [10]. Electrochemical sensors generally consume relatively less power and show relatively high specificity; however, they do not have a long shelf life, consume a large amount of surface area beyond comfortable wearable form factors, and typically do not have sensitivity in the lower ranges of ozone concentration and hence are not practical for the application presented here [10]. Metal-oxide sensors, on the other hand, maintain high sensitivity while being relatively small in comparison and have a much longer shelf life. The drawbacks of metal-oxide sensors, which will be addressed later, are the extra power required to heat the sensing element and the broad selectivity. Operating at high temperatures increases the reaction speed on the sensing surface enabling fast detection of low concentrations of ozone and desorption of gas for recovery of the sensor. Additionally, metal oxides are more sensitive to ambient humidity at lower temperatures. [11]. As a starting point for our environmental sensing, a commercial metal-oxide sensor (Model MICS2614, SGX Sensortech (IS) Ltd., Essex, U.K.) was selected.

Typically, changes in ozone concentration are seen to be relatively slow in the time domain, thereby requiring a lower sampling rate for measurements. Therefore, duty cycling can be implemented to conserve power consumption by turning off the sensor's heater when not in use according to the action re-

quired from the ozone sensor. In the current working scheme of the MICS2614, we define three different states for the sensor: preheat, idle, and measurement. For measurement, while MICS2614 has a sufficiently quick response time of approximately 30 s, there is a relatively long period of time required to initially preheat the sensor once turned on. If the heater is supplied, the recommended dc current of 34 mA, the preheat period is on the order of 20 min. During the preheat state, we oscillated the current supplied to the heating element at a frequency of 2 kHz with various duty cycles to optimize the preheat time versus the average current as seen in Fig. 7. As presented in the next section, we found that an increase in the duty cycle beyond 40% did not significantly changed the preheat period. Once the ozone sensor has finished the preheat cycle, the microcontroller was used to toggle between idle and measurement states. In the idle state, the heater current pulses at the optimized duty cycle of 40% to keep the heater very close to its optimum temperature due to retention of the heat. This translates to the sensing element desorbing gas at a rate just below optimal. Once it is time for a measurement, the heater current switches to a dc signal, requiring only a small amount of time to reach optimal measurement heat due to the retention of heat during the idle state.

As seen in Fig. 8, we have used the introduction of the idle state as a system-level approach to lower the power consumption. However, even with this improvement in the power consumption, it is still far above the required threshold for a system capable of continuous measurement. In order to further reduce
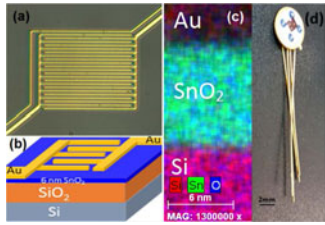
Fig. 9. ALD SnO$_2$ sensor: (a) optical microscope image, (b) 3-D model of structure, (c) Energy-dispersive X-ray spectroscopy map of sensor cross section and (d) sensor mounted on header for system integration.
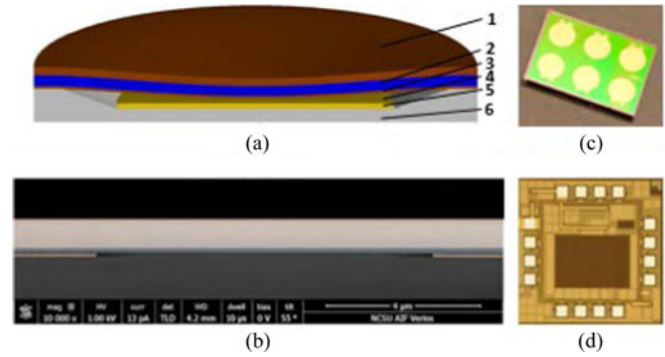

Fig. 10. (a) Cross-sectional schematic of a single CMUT cell With the following layers: 1) Gold top electrode; 2) single-crystal silicon vibrating thin plate; 3) silicon nitride insulation layer; 4) vacuum gap; 5) gold bottom electrode; 6) glass substrate. (b) SEM cross section of the post region between two CMUT cells out of hundreds connected in parallel to form a single large area mechanical resonator. (c) A 6-channel CMUT sensor with a 7×9 mm^2 die area. (d) Micrograph of the custom frontend IC with a 1.5×1.5 mm^2 die area.

the power consumption, we developed a metal-oxide sensor using atomic layer deposition (ALD) that implements an SnO$_2$-based thin film sensor operating at room temperature and is sensitive to ozone concentrations below 50 ppb. We used an interlocking finger design to maximize the surface area with a cross-sectional view presented in Fig. 9. The SnO$_2$ sensing layer was deposited on oxidized silicon (1 0 0) using an ALD system (Model Savannah S100, Cambridge Nanotech, Waltham, MA, USA) with tetrakis (dimethylamino) tin precursor and O$_3$ reactants at 200 °C. The films were annealed at 400 °C in N$_2$ for 3 min to achieve the rutile crystalline phase. Lastly, interdigitated electrodes were deposited via e-beam evaporation with 10 nm of Ti for adhesion followed by 200-nm Au [12].

Temperature and humidity conditions can also cause a change in the resistance of the sensing element in addition to ozone concentration. In order to account for these external conditions as well as to further monitor the environment, an additional sensor (Model SI7023, Silicon Labs, Austin, TX) was implemented to observe temperature and relative humidity. Having dimensions of $3 \times 3 \times 1.2$ mm^3, this sensor outputs two analog voltages, one for temperature and the other for relative humidity. We used a similar sampling rate for the ozone, temperature, and relative humidity sensing. The resistance change of the sensing element due to the temperature and humidity is calibrated using the formula provided by SensorTech [13], while a similar formula has empirically been developed for our custom ozone sensor.

2) Volatile Organic Compounds: Similar to the ozone sensors discussed in the previous section, the commonly used commercially available VOC sensors are based on metal-oxide sensing materials that require heating and as a result consume high power. Another shortcoming of the currently available commercial VOC sensors is that in general they report on total VOCs and lack the specificity to distinguish between different types of VOCs. To enable a detailed study of the correlation between personal VOC exposure and the risk of developing and/or exacerbating asthma, we have developed a custom low-power sensor with high selectivity to different types of VOCs. Our sensor is based on the use of a capacitive micromachined ultrasonic transducer (CMUT) array. In this implementation, the CMUT acts as an electrostatically actuated mechanical resonator (see Fig. 10) to implement a mass sensor, which we transform into a chemical sensor by functionalizing the surface with a thin polymer coating. When target gas molecules are adsorbed at the surface of the polymer functionalization layer, the mass of
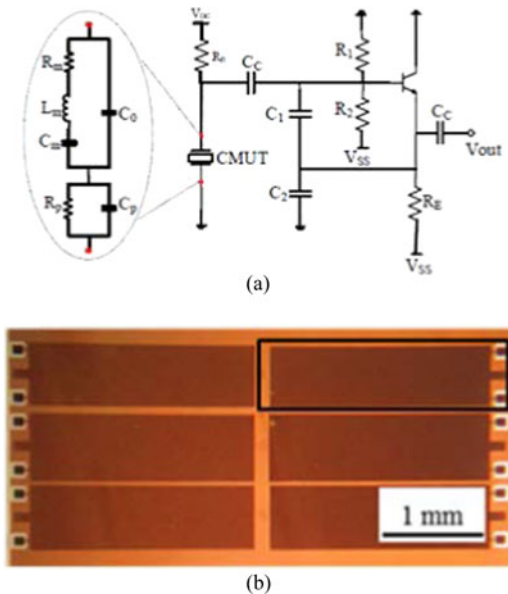

Fig. 11. (a) Schematic of the Colpitts oscillator. (b) A group of CMUT resonators [33].

the mechanical resonator increases and the mechanical resonant frequency shifts down. By using this mechanical resonator as the frequency selective component of an electrical oscillator, one can track the frequency shift resulting from adsorbed gas molecules on the sensor surface. Using an array (see Fig. 10) instead of a single sensor enables the use of a variety of polymers, preferably orthogonal to each other in their selectivity to different VOCs so that we can discriminate between various VOCs by using classification algorithms. Use of an unfunctionalized reference channel in this configuration enables correction for drift and changes in temperature, pressure, and humidity.

In the described sensor implementation, the electrical oscillator (see Fig. 11) is the only power-consuming component. By choosing the operating frequency in the low-megahertz regime, we can minimize the power consumption and still be able to

detect VOCs in the environment in the required high-ppb-to-low-ppm level of concentrations. We designed and implemented a custom integrated circuit (IC) in a $0.18-\mu m$ BiCMOS process to interface with the CMUT resonators (see Fig 9). This custom test IC includes two types of electrical oscillators for testing, a Colpitts oscillator and an inverter-based oscillator, as well as a sine-to-square-wave converter and a digital frequency counter to communicate the frequency shifts as a digital code to the SoC.

The CMUT arrays used in this sensor configuration are fabricated using a three-mask process by utilizing anodic bonding [14]. In this process, the bottom electrode for CMUT elements is implemented using a patterned metal (Cr/Au) layer deposited inside a submicron vacuum-sealed cavity on an insulating glass substrate (see Fig. 10). The device layer of a silicon-on-insulator (SOI) wafer anodically bonded on the glass wafer forms the vibrating plate of the CMUT and allows good control over thickness and uniformity of the plate structure. Anodic bonding provides the benefits of a low cost and low-temperature processing. The use of a patterned bottom electrode minimizes the parasitic series resistance and parasitic shunt capacitance.

B. ECG and Skin Impedance

The traditional systems for heart-rate detection in clinical settings rely on conductive electrolyte-loaded gel-based electrodes which could potentially provoke skin irritation and are not suitable for long-term applications [15]. Recently, various wearable dry electrodes were proposed where there is still a need to improve the susceptibility to motion artifacts [16], [17]. Concurrent sensing of strain and motion helps correlate the motion artifacts with the motion signals and provides a possible method of reducing the motion artifacts. Moreover, the skin impedance is related to various physiological parameters correlated with the wellness of the subjects, such as skin water content (skin hydration level) [18], emotional arousal levels [19], and glucose concentration [20]. We developed a unique electrode architecture embedded within the chest patch to enable multimodal bioelectrical sensing to simultaneously monitor ECG, skin strain, and skin impedance on the chest.

In order to enable long-term continuous health monitoring, this multimodal electrode structure should be 1) highly compliant to maintain good mechanical and electrical contact with curvilinear and dynamic surfaces of human skin, and 2) highly stretchable, as high as 50%, to accommodate strain associated with daily motions [21]. To achieve these, novel electrodes based on silver nanowires (AgNWs) were adopted in our multifunctional sensor system.

As shown in Fig. 12, we defined three rectangular AgNW electrodes at the corners of the triangular chest patch to serve as surface ECG electrodes. Two adjacent AgNW electrodes around the ECG electrode sense skin impedance to capture changes in the electrical properties of the skin. A three-layer capacitive structure comprising strips of AgNW conductors with a highly stretchable insulator dielectric in-between the electrodes acts as the strain sensor. The resulting stretchable parallel plate
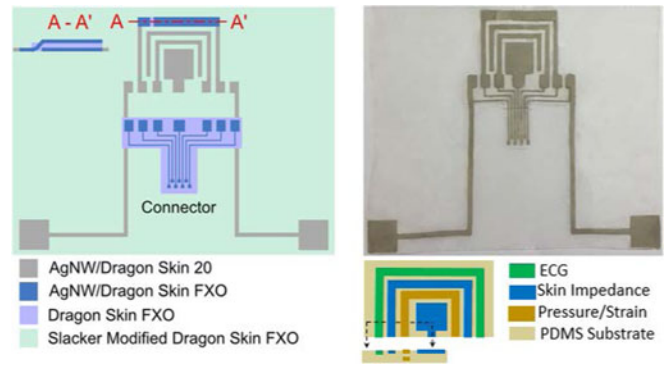

Fig. 12. Silver nanowire based multifunctional patch for ECG, skin impedance and strain sensing: (Left) Schematic illustrations of the AgNW based chest patch and AgNW based extension connector used to connect the patch to the circuitry. (Right-top) A picture showing the fabricated patch with AgNW extension connector attached. (Right-bottom) Around ECG electrode on the top, two inner adjacent electrodes are used for skin impedance sensing and two outer electrodes are used for capacitive strain/motion detection.
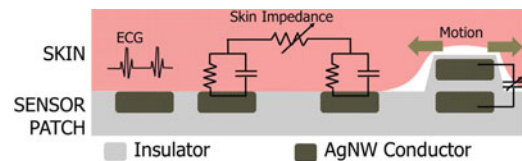

Fig. 13. Schematic description of the sensing schemes of the custom multimodal bioelectrical measurement electrode.

capacitor elongates under a tensile strain such that the distance between the two electrodes decreases, leading to an increase in capacitance. The electrode interaction is further explained by the schematic in Fig. 13.

To fabricate the patch, we first patterned AgNWs which were then inlaid just below the surface of a stretchable insulating polymer (Dragon Skin, Smooth-On, Inc., stretchability > 500%) to form the compliant electrodes. We covered the areas surrounding the AgNW electrodes using slacker-modified Dragon Skin FXO (Smooth-On, Inc.) to provide a self-adhesive and stretchable substrate and thus facilitate the attachment to the skin. Since strain sensors have a three-layer structure, we fabricated its bottom electrode with the other electrodes for ECG and skin impedance while fabricating the strain sensor top electrode separately. We then attached this top electrode to the bottom electrode in the patch using Dragon Skin FXO as a glue to form AgNW/Dragon Skin FXO/AgNW sandwich structure. The top electrode was then attached at point A while remaining isolated from the bottom electrode (see Fig. 12). Finally, we defined an AgNW-based extension connector to connect the sensor patch to the circuit board.

To interface the sensor patch to the circuit boards, we designed a three-piece connector system including 1) an AgNW-based stretchable extension connector connected to the sensor patch (see Fig. 12), 2) a flexible flat cable (FFC) on the PCB and 3) an intermediate adapter using patterned copper traces on a Teflon substrate connecting the extension connector on one end using silver epoxy and the narrower pads within the FFC connector on

the other end. We enclosed the circuit board and connectors in a 3-D printed box, both to be adhered to the center of the chest patch.

The front-end circuit to acquire the ECG-based heart-rate consists of a standard instrumentation amplifier (AD8232, Analog Devices) with a gain of 100 in three-lead configuration and the output is subsequently filtered and amplified via an active second-order band-pass filter. While instrumentation amplifiers usually have good common mode rejection, a driven ground circuit is used to increase this rejection [22]. This driven ground mostly aids in eliminating low-frequency noise that acts as an injected dc bias. The implementation of this driven ground necessitates a third electrode, sacrificing some surface area for a much more motion resilient ECG system. We used Analog Devices' AD5933 impedance converter system to perform impedance spectroscopy for assessing skin impedance and determine capacitance change from strain sensor due to motion. To reduce the power consumption, we also used the ECG and impedance spectroscopy front ends within the MUSEIC chip from IMEC in Belgium [23] that was made available to us through a special evaluation agreement. The MUSEIC ECG circuit combines an ultra-low-power instrumentation amplifier with appropriate filters in a very small size.

C. PPG

To accommodate for the conditions where motion and muscle artifacts override the ECG signal, we decided to add an alternative way to measure heart-rate variability: an optical PPG sensor incorporated into both the wristband and chest patch. The ECG measurements are based on the assessment of the biopotential distribution around the chest caused by the depolarization of the heart muscle tissue during the contraction while the PPG uses the interaction of the photons with the hemoglobin within the contracting and expanding arteries as a result of heart contraction. The PPG sensor is in the form of a probe that has two LEDs of the same wavelength and a single photodiode. This photodiode (APDS-9008, Avago Technologies, San Jose, CA) is selected partly because of its relatively slow response time, which imitates a low-pass filter. An ultra-low-power oscillator is used in conjunction with an analog switch to drive the two LEDs. Our previous work employed a proximity detector as a photodiode and LED driver and used red and infrared wavelengths [24]. While having two wavelengths would allow for the calculation of arterial oxygen saturation and local tissue oxygenation measurements [25], this paper only focuses on the volumetric measurement of blood by performing PPG to calculate heart rate variability, which allows for much lower power consumption with respect to pulse oximetry. Additionally, by implementing PPG at both the chest and the wrist, a measurement of the speed of arterial pulses can be obtained, known as pulse transit time (PTT), which correlates well with mean arterial pressure; this allows for a continuous measurement of blood pressure (see Fig. 14) [26], [27]. Furthermore, the PPG signal at the chest contains oscillations modulated both by cardiac contraction and the respiratory movement of the chest due to the simultaneous absorption of the near infrared light by the
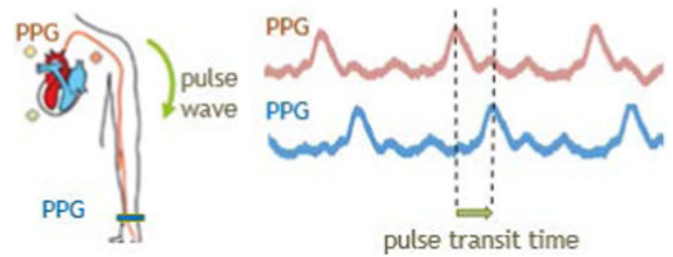

Fig. 14. Diagram describing the PTT and the sample data obtained through the presented chest-patch and wristband.
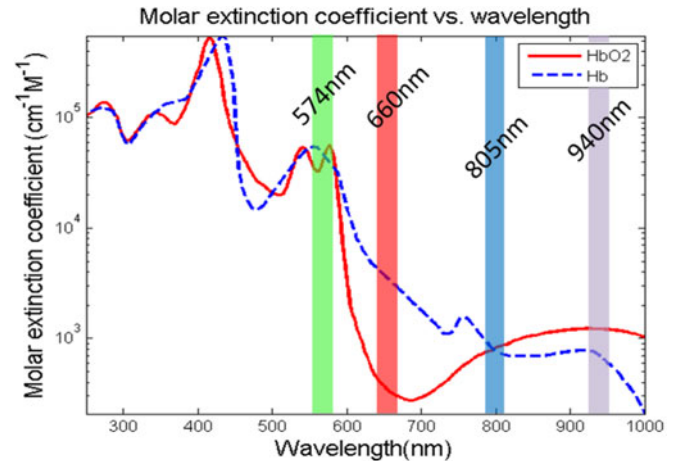

Fig. 15. Graph of the absorption spectra of oxyhemoglobin and deoxyhemoglobin. Note that the typical wavelengths of red and infrared allow for oxygenation as there is differentiation between the two hemoglobin chromophores. However, it can also be seen that green wavelengths are more highly absorbed.

arteries and the veins. Therefore, we used this fact to monitor the respiratory rate in addition to the heart rate.

The typical wavelengths used in PPG systems are red and infrared due to their relatively high penetration in tissue. However, in an effort to lower the power consumption, a green wavelength (see Fig. 15) was selected to increase the signal-to-noise ratio (SNR) and allow for a lower power requirement [28], [29].

In both the wristband and chest patch, the target arteries are relatively close to the surface of the skin. This necessitates a proximal distance between the LEDs and the photodiode, which was selected as 6.5 mm for both devices. Our previous work has shown the use of PPG to be successful with the radial artery in the wrist [28] and other literature has shown PPG to be compatible with the chest region [30]. In order to minimize the movement of the optical probe, we placed a double-sided film (Tegaderm, 3M, Saint Paul, MN) on top of the probe, offering adhesion to the tissue and simultaneously allowing breathability of the skin.

D. Accelerometer and Microphone

Three-axis accelerometers (ADXL362, Analog Devices Inc., Boston, MA, USA) allow for an estimation of movement in both the chest patch and the wristband. As will be discussed in the next section, this is important for further removing motion artifacts from the data. Assuming the ECG electrodes and PPG probes are securely attached to the skin, the motion-induced
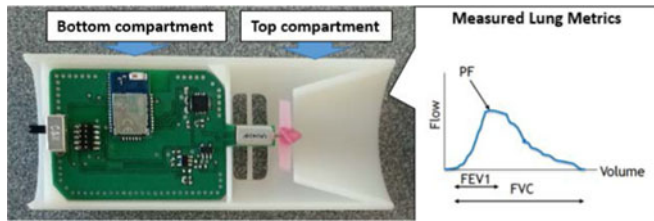
Fig. 16.   (Left) Picture of the custom, handheld spirometer with the description of the measured parameters. The bottom compartment insulates the circuitry from the outside environment while the top compartment exposes the miniature turbine to the airway. Exhaust vents allow for no back pressure to form while blowing into the device. (Right) A typical spirogram and the three relevant parameters. FEV1 is the integral from 0 to 1 s; PEF is the maximum flow rate; FVC is the integral of the entire waveform.

deformation of the arteries and subsequent altered photon path length correlate directly with the accelerometer output in the case of PPG; whereas the motion artifacts in ECG are mainly attributed to concurrent EMG signals of the chest muscles in addition to the strain. These EMG signals are precursors to the measured motion, and thus there exists a strong correlation between the inertial measurements and the induced noise in the ECG signal.

Measurements of wheezing have been shown to be a strong indicator of the amount of airway obstruction present in a patient's respiratory system [31]. By recording this metric, our system can have direct knowledge about the user's lung functionality and how ozone, ambient temperature and humidity, VOCs, heart rate variability, respiratory rate variability, and activity affect the upper airway condition. For this purpose, an MEMS microphone (SPH0641LM4H-1, Knowles, Itasca, IL, USA) with an integrated amplifier was placed in the patch in contact with the tissue and the data were sampled at 2 kHz to detect wheezing sounds.

E. Spirometer

In order to have a direct measurement of lung function that is synchronized to the other physiological and environmental measurements, a handheld spirometer was designed by using a COTS sensor and a novel spirometry technique. As the COTS sensor, we used a pressure-based flow sensor (AWM720P1, Honeywell, Morris Plains, NJ, USA). In order to reduce the power consumption of this system, a novel spirometry method was developed using a miniature turbine. This custom spirometer incorporates a printed circuit board that is enveloped by two identical ABS plastic clamshell lids (see Fig. 4). As seen in Fig. 16, two compartments are formed by the shell: a bottom compartment comprising of the majority of the circuit components and a top compartment that houses the miniature turbine and is exposed to the environment. Airflow from the user's exhaled breath travels past the miniature turbine before exiting the exhaust ports. The flow of air propels revolutions from the turbine that is analogous to the flow rate and produces a corresponding voltage. Additionally, an accelerometer is used to estimate the posture of the user, as altered positions of the diaphragm can affect the volume within the lung.

As spirometry is typically a coached procedure, a smartphone application was developed to guide the patient through the correct breathing protocol. Once the user powers on the device, the smartphone application establishes a connection with the spirometer and begins sending posture and airflow measurements. The patient is then guided through three breathing procedures and the average PEF, FEV1, and FVC are recorded and pushed to the dedicated server. After this short procedure, the patient can then turn off the spirometer until the next usage. While this device does not demonstrate the same continuous monitoring methodology as the wristband and chest patch, it is a prime example of the integration of measurements that cannot be ideally measured in a continuous fashion.

F. Microcontroller and Transceiver

To achieve wireless connection with a nearby data aggregator within a range of 10 m, we used a COTS SoC (CC2541, Texas Instruments, Dallas, TX, USA) on the chest-patch, wristband, and spirometer. CC2541 combines an 8051 microcontroller with radio-frequency transceiver in 6×6 mm^2, while providing 8 KB of RAM and up to 256 KB of flash memory. CC2541's 21 general-purpose I/O pins and onboard 12-bit ADC allow for simultaneous acquisition from multiple sensors. It has ultralow-power sleep modes and short transition times between operating modes, which can be used to further decrease the power consumption. It also provides tailored software for use with Bluetooth standards to establish connections with computers and smartphones. An additional discussion about the custom SoC designed under ASSIST Center is provided in Section V.

IV. RESULTS

In this study, we present preliminary results that show the wearability and functionality of each of the discussed sensor subsystems and the resulting power consumption. This proof of concept is limited to the ability of each of the sensors to produce reasonable preliminary output in controlled environments under protocols approved by the Institutional Review Board of University of North Carolina at Chapel Hill and carried out in specialized physiology and environmental exposure facilities located at the EPA Human Studies Facility in Chapel Hill by our medical team at the UNC Center for Environmental Medicine, Asthma and Lung Biology. The physiology laboratory allows for assessment of minute ventilation during exercise with state-of-the-art spirometry and standard ECG telemetry. The environmental exposure facility brings this technology to an ozone chamber that allows for simultaneous exercise and exposure to ozone, mimicking an ambient air pollutant exposure event. Future work will extend these results to the analyzing of induced exacerbations in normal and asthma populations in these environments where activity levels and ozone exposure can be regulated.

A. Ambient Gas Sensing

1) Ozone: By using a current pulsing scheme with the COTS ozone sensor, the average power consumption of the heater was
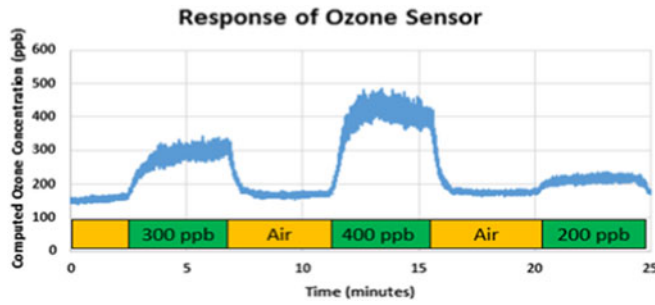
Fig. 17. Response of the MICS2614 metal oxide ozone sensor to various concentrations of ozone. The sensor outputs an analog voltage which is then translated into a measure of concentration by the BLE connected peripheral device.
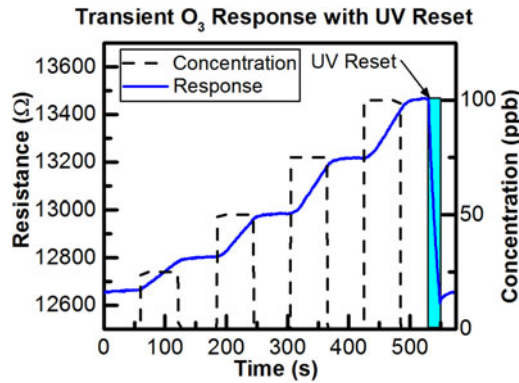

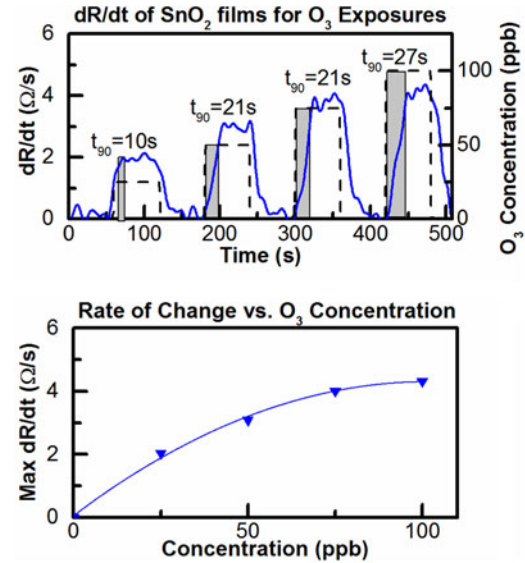Fig. 18. Transient response of SnO_2 sensor to ozone exposure and UV recovery.

Fig. 19. Top dR/dt versus time for 25-, 50-, 75-, and 100-ppb ozone exposure and (bottom) dR/dt vs concentration.

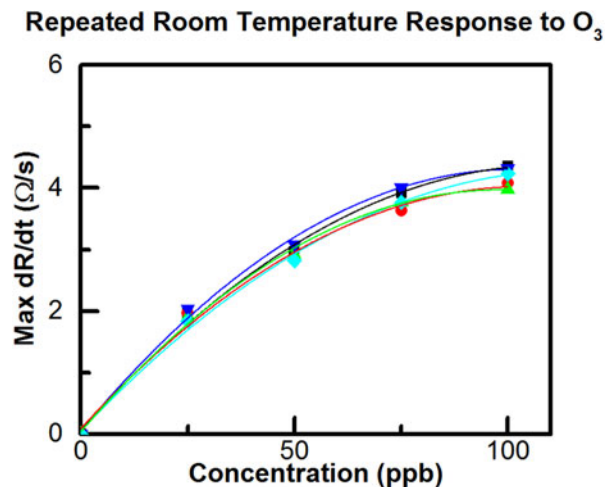Fig. 20. Response to repeated exposures to 25-, 50-, 75-, and 100-ppb O_3.

more than halved during idle periods (see Fig. 8). As the ozone sensor has a response time of 30 s, the Nyquist criterion dictates a sampling frequency of at least 66 mHz. Using this power scheme, the average current drawn over a relatively long period of time is 15.65 mA as opposed to 34 mA when an idle state is not implemented causing a reduction of power from 102 to 46.95 mW while still maintaining integrity of the sensor (see Fig. 17). The COTS temperature/humidity sensor has a power consumption of 0.45 mW, which was reduced to 0.225 mW after duty cycling.

The ALD-fabricated 7-nm ultrathin film SnO_2 metal-oxide sensors demonstrate room temperature operation for ultra-low-power consumption of $150\ \mu W$, as previously reported [12]. We have tested responses to three different environmental pollutants: CO (50 ppm), NO_2 (100 ppb), and O_3 (100 ppb) using an NIST-certified ozone generator (T700U, Teledyne, Thousand Oaks, CA, USA) and a custom built testing chamber in order to test the ozone response and false positives from CO and NO_2. The concentrations were chosen to cover typical atmospheric levels of 0–50-ppm CO and 20–100-ppb NO_2. The sensors are not heated and thus response to ozone and especially recovery in clean air are relatively slow. Short exposures to UV light rapidly desorb O_3 molecules enabling sensor recovery. The transient response to ozone exposure and UV recovery can be seen in Fig. 18.

Due to the slow response and lack of saturation, it is difficult to see the response time and magnitude in Fig. 18; however,

the time derivative of the resistance change (dR/dt) upon ozone exposure can be evaluated to rapidly obtain the ozone concentration as previously reported in the literature [32]. Fig. 19 shows the relationship between dR/dt and ozone concentration is approximately linear, while Fig. 20 shows the sensor is reliable and repeatable, giving similar results for repeated 100-ppb exposures. In fact, the sensor lifetime currently under test shows the sensor is still responding to ozone six months later and continues to be tested intermittently.

Finally, selectivity of the sensor was evaluated by exposing it to typical or high concentrations of NO_2 and CO as seen in Fig. 21. Again dR/dt has been evaluated for gas exposure and no response is seen to 50-ppm CO or to 100-ppb NO_2. Response to 100-ppb O_3 remains clear indicating good selectivity toward these gases at atmospheric concentrations.
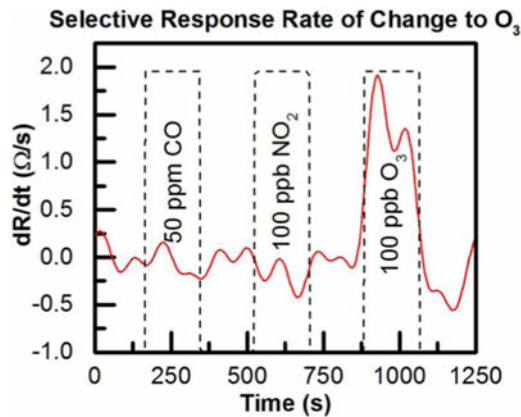
Fig. 21. ALD SnO_2 sensor response to 100 ppb O_3 showing selectivity versus 50 ppm CO and 100 ppb NO_2 [12].
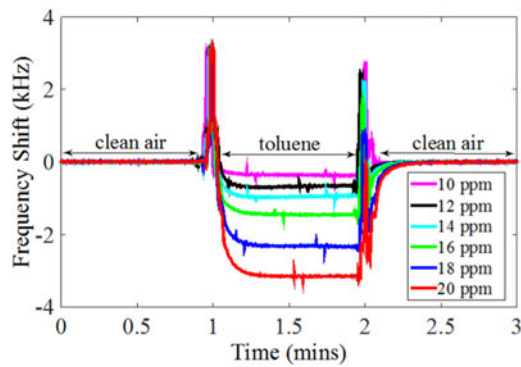

Fig. 22. Chemical test results showing the response of a single PIB-coated channel to toluene vapor.

While the power consumption of this room temperature ozone sensor is in the nanowatt range (300 nW), the power required to reset the sensor using UV light must also be accounted for. By pulsing the UV LED at a 1% duty cycle, the average power consumption of the ozone sensor becomes approximately 150 μW [12]. This is a steep decrease in power consumption when compared to commercial metal-oxide sensors (including the one with our system optimizations) illustrating that this sensor has strong potential in wearable systems.

2) Volatile Organic Compounds: We tested the CMUT-based low-power VOC sensor as a standalone submodule using a calibration vapor generator (Model OVG-4, Owlstone Inc., Cambridge, U.K.). For initial testing, we used a 4.52-MHz device (Q = 180) coated with a thin layer of polyisobutylene (PIB) and demonstrated an average sensitivity of 270 Hz/ppm within the range of 10–20 ppm of toluene concentration and a resolution of 12 ppb (see Fig. 22) [33]. We have also implemented 6-, 8-, and 15-channel prototype arrays with a standard deviation of 1% in the parallel resonant frequency (4.5 MHz) in a 7×9 mm^2 die area. Toward the demonstration of improved selectivity of our array-based sensor approach, we performed initial tests with three channels. In these experiments, measured response of three channels, one uncoated, one with a PIB layer, and one with a polyvinyl alcohol (PVA) layer, to 20-ppm

toluene vapor showed 1:13:37 ratio in the response of reference:PVA:PIB channels [34].

Further experiments with a wider range of concentration and different analytes are in progress. We have also demonstrated a complete end-to-end system wherein the custom front-end IC as interfaced with a 3.6-MHz CMUT and the digital equivalent of the frequency value is read serially [35]. With a 0.1-s start-up time, 1-s measurement time, less than 1-ms read time, and one measurement every minute the complete system's power consumption is 10 μW, when operated from a 1.8-V supply.

B. ECG and Skin Impedance

Due to the high compliance and self-stickiness of the polymer substrate, the chest patch can self-adhere to the skin, but we used a Tegaderm Film for extra adherence. We designed the electrode part of the patch to be disconnected from the circuit box and disposed after one week of use. Both the patch adhesive material and the Tegaderm Film support one week of attachment to skin without any mechanical problems. The preliminary biocompatibility experiments suggest that the AgNWs concentration used should not cause skin issues or risks for continuously wearing for this duration.

ECG signals were obtained when a subject was first asked to stand still and then swing arms. Motion artifacts were observed due to the changing electrical contact between the AgNW electrode and the skin under motion (see Fig. 23). Adaptive filtering methods can be used to reduce the motion artifact but requires additional information from the strain/motion sensing. For strain sensing, impedance from the strain sensor was first measured and then converted to capacitance. Fig. 23 presents the capacitance change when the subject was at rest, extending arms and performing repeated cycles of extending arms and then relaxing. The gauge factor (GF), defined as the relative change in capacitance divided by the mechanical strain, can be used to relate the capacitance change and the actual strain. When the GF for this capacitive strain sensor was calibrated to be 1, the average strain associated with several cycles of arm extension was around 8%. While this measurement of strain could potentially be used for motion artifact removal on the ECG data, the biggest contribution of an impedance measurement is in the correlation with skin hydration. In order to test the functionality, a moisturizing lotion was used as a way to change the skin impedance. Changes in skin hydration level/skin water content result in changes in the dielectric constant and conductivity of the skin, and thus the skin impedance [36]. As shown in Fig. 23, the lotion applied on the skin increased the skin hydration level and accordingly decreased skin impedance.

The design of the chest patch shape was mostly influenced by the optimal ECG electrode positioning. Initially, we used three electrodes in close proximity centered on the pectoral muscle to allow for a reduction in surface area. However, this led to an ECG waveform with a highly exaggerated T-wave and left the signal very susceptible to motion artifacts. The distance between the electrodes was subsequently increased, resulting in a placement close to the standard V2–V6 lead placement [37]. The driven
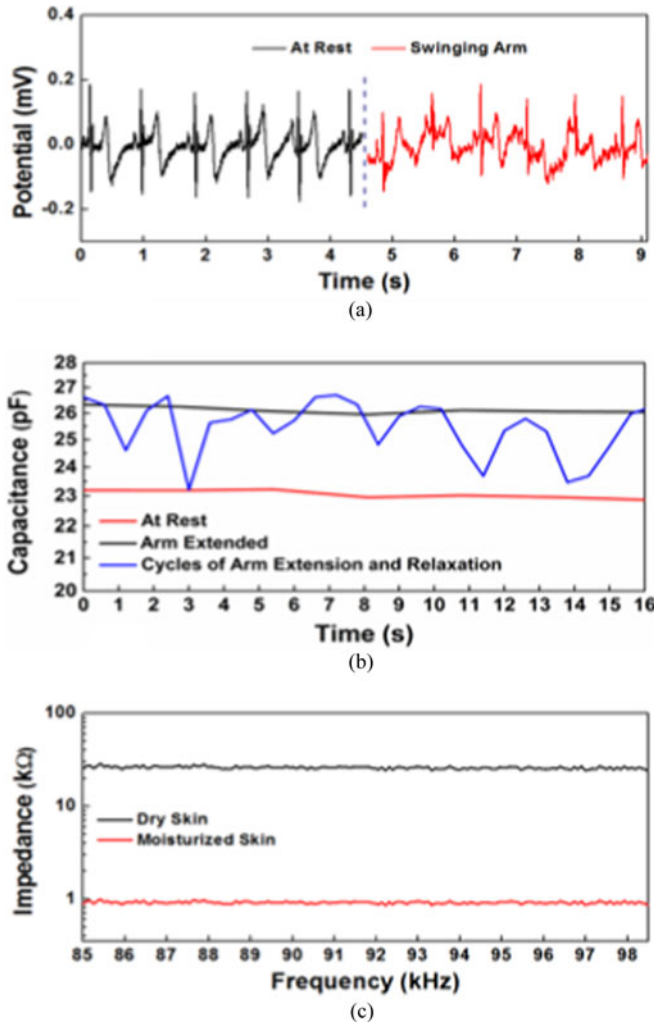
Fig. 23. Multimodal data collected from AgNW based chest patch: (a) ECG signals at rest and under motion. (b) Strain signals detected from strain sensors. (c) Skin impedance obtained for dry and moisturized skin.
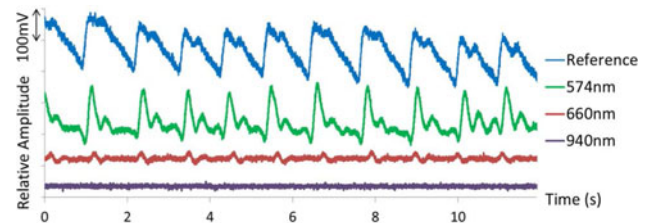

Fig. 24. PPG measurement from radial artery with 0.4 mA sent to LEDs with wavelengths in green, red and infrared regions. The reference waveform was obtained using a standard transmittance finger probe (805 nm).

C. PPG

In order to test the functionality of the PPG probe, it was placed on the wrist and compared against a standard finger clip probe. As seen in Fig. 24, the 574-nm wavelength was the best choice for a reflective measurement at the radial artery, which agrees with the previous literature [29]. In the case of the 940-nm wavelength, the signal was not large enough to be observed over the system's noise. Fig. 15 shows the absorption spectra for oxyhemoglobin and deoxyhemoglobin, showing that 574-nm light is absorbed more readily. This figure also depicts the reason why 574-nm light limits our measurement to PPG as opposed to pulse oximetry, as the two hemoglobin chromophores absorb nearly identical amounts of this wavelength.

While the Tegaderm Film prevented the optical probe from wandering across the surface of the tissue, both the chest and wrist regions are greatly affected by motion due to the force enacted on the arteries themselves. The force of motion causes the cross-sectional area of the arteries to slightly change, affecting the volume of blood in the measurement region [41]. This was handled using the appropriate signal processing techniques as explained later.

In order to achieve a system that can perform continuous monitoring, it is important to ensure the data are not corrupted during the performance of daily-life activities. PPG measurements are notorious for being easily corrupted by motion. Unfortunately, a simple band-pass filter cannot solve this problem, as the noise induced by motion is often very similar in frequency to the desired signal. This requires adaptive filtering, where a certain measured waveform that has a high correlation with the noise is used to distinguish the signal from the noise. In this instance, the accelerometer provides a distinction, as the motion-induced noise correlates well with the experienced acceleration. There are several types of adaptive filtering methods with varying degrees of computational complexity. For this application, the normalized least means square (NLMS) adaptive filtering algorithm [42], [43] was used to remove the noise distortion from the physiological signal where the noise is highly correlated with motion (see Fig. 25). For this study, the raw data were transferred over BLE to the data aggregator where the NLMS adaptive filtering has been performed on the data to be able to record and analyze raw and processed data.

D. Spirometer

As the sensing methodology of our novel spirometer is not standard, there is additional calibration required which falls

ground electrode is less sensitive to placement and is located above the two differentials. In this electrode configuration, the QRS complex is the more dominant wavelet as opposed to the T-wave. The difference between using the QRS complex and the T-wave as a measure of heart rate is a matter of which frequency band is noisier. The band containing the QRS complex is at higher frequency than that of the T wave, around 8 to 20 Hz [38] as opposed to the 2–5 Hz range of the latter [39]. The QRS frequency is typically above the frequency of human cyclic movement, such as normal running, which reflects an EMG-induced noise around 2–3 Hz [40]. Overall, these preliminary results demonstrate the feasibility of monitoring multiple health parameters using a chest patch with the designed multimodal AgNW-based sensors.

AD8232 and AD5933 consumed a combined power amount of 30.17 mW for ECG and impedance measurements. IMEC's MUSEIC chip drastically dropped the average power consumption to 530 μW, with the majority of the saving coming from the alternative method of impedance and ECG sensing [23].
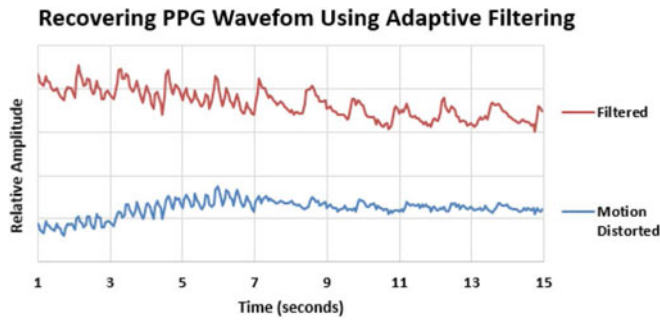
Fig. 25. Motion artifact removal from PPG obtained at the wrist during normal walking gait.
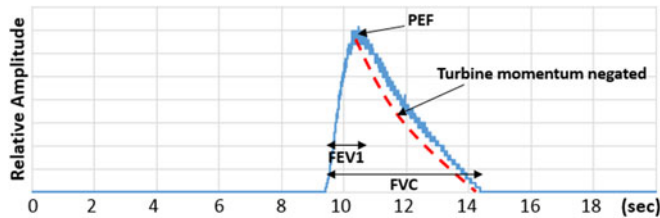

Fig. 26. Sampled output of the custom handheld spirometer during a coached breathing maneuver resembling a typical spirogram. The red dotted line is a visual representation of what the declining waveform looks like once the momentum of the turbine's fan has been accounted for.
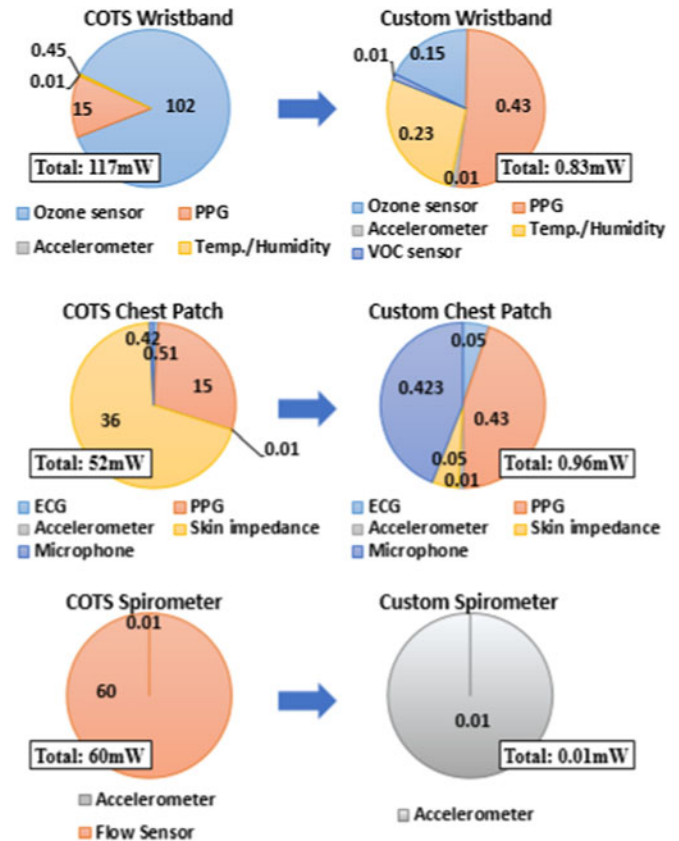

Fig. 27. Comprehensive breakdown of the power sensor consumption of the wristband (Top), the chest patch (Center), and the spirometer (Bottom). The left column represents the systems comprised of COTS sensors; the right column represents the custom ASSIST solutions. The shown data are for sensors and sensor front-end circuits and do not include the SoC and radio. The SoC and radio consume a combined 11.5 mW for each subsystem and reducing this power consumption is underway. All of the listed metrics are in units of mW.

outside the scope of this paper. However, during a coached breathing maneuver, graphs of typical shape were produced as seen in Fig. 26. We are in the process of implementing an algorithm that negates the added momentum of the turbine's fan as well as a transform function to recreate an actual flow measurement. The additional benefit to this custom-built spirometer is the ability to harvest energy from the turbine during an actual measurement. The COTS iteration of this spirometer, incorporating the flow sensor from Honeywell, uses a pressure gradient to measure airflow and consumes 60 mW of power. By utilizing the miniature turbine, the system goes from consuming power to actually generating energy in the millijoule range. It is noteworthy that this spirometer concept won the Consortia for Improving Medicine with Innovation and Technology, Massachusetts General Hospital, Ambulatory Practice of the Future (CIMIT-MGH-APF) national Prize for Primary Healthcare in 2014.

E. Overall System and Other Components

The selected accelerometer and microphone were already low power (0.05 and 0.42 mW, respectively) and we kept these components when we were replacing the other higher power consuming sensors and sensor interface circuits. The sensors and the supporting front-end circuit part of the chest-patch, wristband, and the spirometer prototypes assembled using COTS components consumed a total of 52, 117, and 60 mW, respectively. The system level optimization and custom fabricated nano-enabled ASSIST sensors brought this power down to 0.96, 0.82, and 0.01, mW respectively (see Fig. 27). This can be further reduced

Fig. 28. Demonstration of the simultaneous acquisition of ECG, PPG and accelerometer signals while the subject is moving on a treadmill wearing the presented platforms. Waveform amplitudes have been scaled for graphical purposes.

by adjusting the duty cycling to provide less frequent data. The COTS SoC from Texas Instruments to collect and transmit the data consumed an additional 11.5 mW for each form factor. As summarized in the next section, we are in the process of developing a custom ASSIST SoC to bring this power consumption down to 30 µW [8].

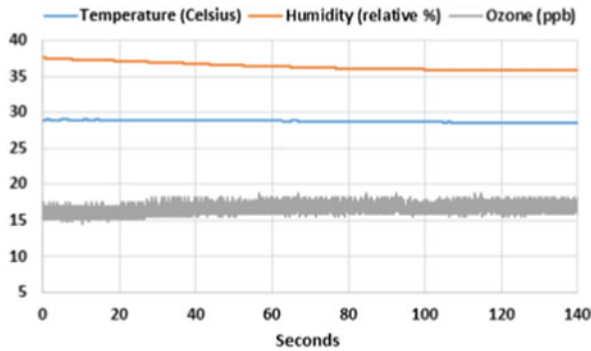Fig. 29. Environmental data obtained through the presented wristband during the experiment where subject is walking on a treadmill.

TABLE I
SAMPLING RATE FOR BLE TRANSMISSION OF SENSING MODALITIES (Hz)

VOC Sensor	Ozone Sensor	Humidity /Temp.	Acceler- ometer	PPG	ECG	Flow Sensor	Mic
0.02	10	10	30	30	50	1k	2k

Fig. 28 shows one of the advantages to having PPG measured at two different locations. Being close to the radial artery, the wrist PPG contained stronger cardiac modulations and was a better indicator of heart rate. The chest patch PPG had a stronger correlation with the respiratory movement and provided the respiratory rate. While Fig. 28 demonstrates some of the simultaneous acquisition of physiological parameters, Fig. 29 shows some of the environmental data collected, both of these data sets from a patient walking on a treadmill in a controlled clinical setting.

V. DISCUSSION AND CONCLUSION

The vision of the ASSIST Center is to utilize nano-enabled low-power sensors, low-power computational and communication circuits, and energy harvesting devices from body heat and motion [8]. These technologies are used for designing wearable and wireless systems for data collection for multimodal and simultaneous sensing of human physiology, behavior, and environment for correlation and subsequent wellness management. The scope of this paper is to highlight the Center's efforts particularly on sensor and system optimization for correlating environmental exposure (ozone, VOCs, humidity, temperature) with a number of physiologic parameters (heart rate variability, respiratory rate variability, wheezing, hydration, and activity levels). These parameters and their associated sampling rates (see Table I) were selected after discussion with a panel of clinicians that suggested that asthma management was an appropriate and significant use case for our wearable systems.

Asthma is one of the most common chronic respiratory diseases in the United States. Current management of this disease is based on patient recall, review of prescription refills, and periodic caregiver evaluation. Real-time, objective measures of physiologic parameters, medication use, patient-reported outcomes, and environmental measures would greatly enhance management of chronic and acute asthma. We hypothesize that wearable sensor arrays linked to data aggregators (such as a

smartphone) would allow for real-time monitoring of disease. Barriers to development of unobtrusive sensor arrays include excessive power consumption and component design that impedes wearability of the array components.

To better assess the design barriers for developing a wearable asthma sensor array, we assembled a prototype multimodal wearable sensor system using state-of-the-art COTS components to analyze power consumption parameters and assess design barriers to achieve device wearability. Subsequent to our initial evaluations, we demonstrated that system-level optimization and novel nano-enabled technologies enabled significantly lower power consumption and improved wearability of sensor components. This was a crucial initial step in addressing the most critical sensor subblocks that impede the development of a continuous monitoring system.

Although the total power consumption was reduced in each device in our system, it will still be necessary to further reduce energy requirements in all three presented form factors. While the focus of this paper was just the sensors and sensor front-end electronics, we would like to highlight that our parallel efforts to enable a custom SoC is in progress and expected to bring overall power consumption to submilliwatt levels [8], [44]–[47]. The collaborative effort within the ASSIST Center will address energy consumption needs by development of low-power systems while using more efficient energy harvesters to supplant batteries as a required power source for the sensor array [8].

Although we continue to pursue further improvements in power requirements and wearability of sensor components, the COTS prototype system described in this report is sufficient to enable us to test sensor performance in assessing the correlation between physiological parameters and exposure to the ozone in healthy and normal volunteers undergoing experimental ozone challenge. The experiments using a newly developed clinical protocol are underway where we collect data from multiple subjects. In this protocol, we ask volunteers to undergo exercise challenge and methacholine challenge (a test for airway reactivity which mimics an acute asthma attack). These tests are being performed at our physiology and environmental challenge facilities [48]. We will use rapid improvement cycles to continuously refine our sensor array systems prior to field-testing in real life settings. This data will then be used to develop of algorithms for the preemptive detection of an asthma attack onset. Even more important than this imminent attack detection is the ability for a physician to review the recorded data and easily identify how ozone and VOC exposure and activity levels affect chronic asthma control.

REFERENCES

[1] Center for Disease Control and Prevention, "Vital Signs: Asthma in the US," *Cent. Dis. Control Prev.*, p. 1, May 2011.

[2] T. A. Barnes and L. Fromer, "Spirometry use: Detection of chronic obstructive pulmonary disease in the primary care setting," *Clin. Interv. Aging.*, vol. 6, pp. 47–52, Jan. 2011.

[3] R. McConnell *et al.*, "Asthma in exercising children exposed to ozone: A cohort study," *Lancet*, vol. 359, no. 9304, pp. 386–391, 2002.

[4] R. J. Delfino *et al.*, "Daily asthma severity in relation to personal ozone exposure and outdoor fungal spores," *Amer. J. Respir. Crit. Care Med.*, vol. 154, no. 3 Pt 1, pp. 633–641, 1996.

[5] U. Nurmatov, N. Tagieva, S. Semple, G. Devereux, and A. Sheikh, "Volatile organic compounds and risk of asthma and allergy: A systematic review and meta-analysis of observational and interventional studies," *Prim. Care Respir. J.*, vol. 22, no. 1, pp. PS9–PS15, 2013.

[6] H. Rhee, S. Miner, M. Sterling, J. S. Halterman, and E. Fairbanks, "The development of an automated device for asthma monitoring for adolescents: Methodologic approach and user acceptability," *JMIR mHealth uHealth*, vol. 2, no. 2, Jun. 2014, Art. no. e27.

[7] H. Chu, C. Huang, Z. Lian, and J. J. P. Tsai, "A ubiquitous warning system for asthma-inducement," in *Proc. IEEE Int. Conf. Sens. Netw., Ubiquitous, Trustworthy Comput.*, 2006, pp. 186–191.

[8] V. Misra *et al.*, "Flexible technologies for self-powered wearable health and environmental sensing," *Proc. IEEE*, vol. 103, no. 4, pp. 665–681, Apr. 2015.

[9] "NC state to lead NSF nanosystems engineering research center on self-powered health monitoring," *NC State News Ser.*, (2012). [Online]. Available: https://news.ncsu.edu/2012/09/ndassist/

[10] K. Arshak, E. Moore, G. M. Lyons, J. Harris, and S. Clifford, "A review of gas sensors employed in electronic nose applications," *Sens. Rev.*, vol. 24, no. 2, pp. 181–198, 2004.

[11] G. Korotcenkov and B. K. Cho, "Ozone measuring: What can limit application of SnO 2-based conductometric gas sensors?," *Sens. Actuators B, Chem.*, vol. 161, no. 1, pp. 28–44, 2012.

[12] S. Mills, M. Lim, L. Bongmook, and V. Misra, "Atomic layer deposition of SnO_2 for selective room temperature low PPB level O_3 sensing," *Solid State Sci. Technol.*, vol. 4, pp. S3059–S3061, 2015.

[13] SGX, "MiCS-2614 Datasheet," pp. 1–5.

[14] F. Y. Yamaner, X. Zhang, and O. Oralkan, "A three-mask process for fabricating vacuum-sealed capacitive micromachined ultrasonic transducers using anodic bonding," *IEEE Trans. Ultrason.*, vol. 62, no. 5, pp. 972–982, May 2015.

[15] W. Uter and H. J. Schwanitz, "Contact dermatitis from propylene glycol in ECG electrode gel," *Contact Dermatitis*, vol. 34, no. 3, pp. 230–231, Mar. 1996.

[16] A. C. Myers, H. Huang, and Y. Zhu, "Wearable silver nanowire dry electrodes for electrophysiological sensing," *RSC Adv.*, vol. 5, no. 15, pp. 11627–11632, 2015.

[17] M. K. Yapici, T. Alkhidir, Y. A. Samad, and K. Liao, "Graphene-clad textile electrodes for electrocardiogram monitoring," *Sens. Actuators B, Chem.*, vol. 221, pp. 1469–1474, 2015.

[18] X. Huang, W.-H. Yeo, Y. Liu, and J. A. Rogers, "Epidermal differential impedance sensor for conformal skin hydration monitoring," *Biointerphases*, vol. 7, no. 1–4, pp. 1–9, 2012.

[19] M. van Dooren, J. J. G. G.-J. de Vries, and J. H. Janssen, "Emotional sweating across the body: Comparing 16 different skin conductance measurement locations," *Physiol. Behav.*, vol. 106, no. 2, pp. 298–304, May 2012.

[20] A. Caduff, E. Hirt, Y. Feldman, Z. Ali, and L. Heinemann, "First human experiments with a novel non-invasive, non-optical continuous glucose monitoring system," *Biosens. Bioelectron.*, vol. 19, no. 3, pp. 209–217, Nov. 2003.

[21] S. Yao and Y. Zhu, "Wearable multifunctional sensors using printed stretchable conductors made of silver nanowires," *Nanoscale*, vol. 6, pp. 2345–2352, 2014.

[22] V. Acharya, "Improving common-mode rejection using the right-leg drive amplifier," *Application Rep. SBAA188*, Texas Instruments, 2011.

[23] N. Van Helleputte *et al.*, "18.3 A multi-parameter signal-acquisition SoC for connected personal health applications," in *Proc. IEEE Int. Solid-State Circuits Conf. Dig. Tech. Pap*, vol. 57, 2014, pp. 314–315.

[24] J. P. Dieffenderfer *et al.*, "Wearable wireless sensors for chronic respiratory disease monitoring," in *Proc. IEEE 12th Int. Conf. Wearable Implantable Body Sens. Networks*, 2015, pp. 1–6.

[25] J. P. Dieffenderfer, M. C. Bair, and A. Bozkurt, "Towards a smart bandage with functional near infrared spectroscopy capability," in *Proc. IEEE Conf. Biowireless*, vol. 4, 2013, pp. 13–15.

[26] P. Fung, G. Dumont, C. Ries, C. Mott, and M. Ansermino, "Continuous noninvasive blood pressure measurement by pulse transit time," in *Proc. IEEE Eng. Med. Biol. Soc.*, vol. 1, 2004, pp. 738–741.

[27] R. Mukkamala *et al.*, "Toward ubiquitous blood pressure monitoring via pulse transit time: Theory and practice," *IEEE Trans. Biomed. Eng.*, vol. 62, no. 8, pp. 1879–1901, Aug. 2015.

[28] J. P. Dieffenderfer *et al.*, "Solar powered wrist worn acquisition system for continuous photoplethysmogram monitoring," in *Proc. IEEE Eng. Med. Biol. Soc.*, 2014, pp. 3142–3145.

[29] V. Vizbara, "Comparison of green, blue and infrared light in wrist and forehead photoplethysmography," in *Proc. 17th Int. Conf. Biomed. Eng.*, vol. 17, no. 1, 2013, pp. 78–81.

[30] B. Widrow *et al.*, "Adaptive noise cancelling: Principles and applications," *Proc. IEEE*, vol. 63, no. 12, pp. 1692–1716, Dec. 1975.

[31] J. Teeter and E. Bleecker, "Relationship between airway obstruction and respiratory symptoms in adult asthmatics," *Chest*, vol. 113, pp. 272–277, 1998.

[32] C. H. Wu, G. J. Jiang, C. C. Chiu, P. Chong, C. C. Jeng, R. J. Wu, and J. H. Chen,, "Fast gas concentration sensing by analyzing the rate of resistance change," *Sensors Actuators, B Chem.*, vol. 209, pp. 906–910, Mar. 2015.

[33] M. M. Mahmud *et al.*, "A low-power gas sensor for environmental monitoring using a capacitive micromachined ultrasonic transducer," *Proc. IEEE Sensors*, 2014, pp. 677–680.

[34] M. M. Mahmud *et al.*, "A capacitive micromachined ultrasonic transducer (CMUT) array as a low-power multi-channel volatile organic compound (VOC) sensor," presented at the IEEE Sensors Conf., Busan, South Korea, 2015.

[35] M. Kumar, O. Oralkan, B. Floyd, and V. Misra, "A low-power integrated interface circuit for a resonant gas sensor based on a capacitive micromachined ultrasonic transducer (CMUT)," in *Proc. IEEE Sensors*, 2015, pp. 1–4.

[36] S. Yao and Y. Zhu, "Nanomaterial-enabled stretchable conductors: strategies, materials and devices," *Adv. Mater.*, vol. 27, no. 9, pp. 1480–1511, 2015.

[37] K. Khunti, "Accurate interpretation of the 12-lead ECG electrode placement: A systematic review," *Health Educ. J.*, vol. 73, no. 5, pp. 610–623, Apr. 2013.

[38] M. Elgendi, M. Jonkman, and F. Deboer, "Frequency bands effect on QRS detection," in *Proc. Int. Conf. Bio-Inspired Syst. Signal Process.*, Valencia, Spain, 2010.

[39] V. X. Afonso, *Biomedical Digital Signal Processing*. Upper Saddle River, NJ, USA: Prentice-Hall, 1993, pp. 236–264.

[40] G. Musch, "The resonant step frequency in human running," *Pflügers Archiv*, vol. 434, pp. 678–684, 1997.

[41] H. Harry Asada, H.-H. Jiang, and P. Gibbs, "Active noise cancellation using MEMS accelerometers for motion-tolerant wearable bio-sensors," in *Proc. IEEE Conf. Eng. Med. Biol. Soc.*, vol. 3, Jan. 2004, pp. 2157–2160.

[42] T. Tamura, Y. Maeda, M. Sekine, and M. Yoshida, "Wearable Photoplethysmographic Sensors—Past and Present," *Electronics*, vol. 3, no. 2, pp. 282–302, 2014.

[43] G. Morren *et al.*, "Detection of fast neuronal signals in the motor cortex from functional near infrared spectroscopy measurements using independent component analysis," *Med. Biol. Eng. Comput.*, vol. 42, no. 1, pp. 92–99, 2004.

[44] A. Banerjee and B. H. Calhoun, "An ultra-low energy subthreshold SRAM bitcell for energy constrained biomedical applications," *J. Low s Electron. Appl.*, vol. 2, pp. 119–137, 2014.

[45] J. F. Bolus, B. H. Calhoun, and T. N. Blalock, "Low power electronics and applications 39 fJ/bit on-chip identification of wireless sensors based on manufacturing variation," *Low Power Electron. Appl.*, vol. 4, pp. 252–267, 2014.

[46] A. Shrivastava, N. E. Roberts, O. U. Khan, D. D. Wentzloff, and B. H. Calhoun, "A 10 mV-input boost converter with inductor peak current control and zero detection for thermoelectric and solar energy harvesting with 220 mV cold-start and -14.5 dBm, 915 MHz RF Kick-St," *IEEE J. Solid-State Circuits*, vol. 50, no. 8, pp. 1820–1832, Aug. 2015.

[47] E. P. Management, "21.3 A 6.45µW Self-Powered IoT SoC with integrated energy-harvesting power management and ULP asymmetric radios," in *Proc. Int. Solid-State Circuits Conf.*, 2015, pp. 384–386.

[48] Center for environmental medicine, asthma and lung biology. (2016). [Online]. Available: https://www.med.unc.edu/cemalb

Authors' photographs and biographies not available at the time of publication.